



Assessing the efficacy of iron (II, III) oxide nanocomposite for the photodegradation of organic dye pollutants and textile wastewater under UV–visible irradiation

Mahnaz Parastar Gharehlar¹ · Shabnam Sheshmani¹ · Farrokh Roya Nikmaram¹ · Zohreh Doroudi¹

Received: 12 August 2023 / Accepted: 15 November 2023 / Published online: 5 December 2023
© The Author(s), under exclusive licence to the Institute of Chemistry, Slovak Academy of Sciences 2023

Abstract

The existence of artificial dyes in water is a significant environmental concern, as it can lead to poor water quality. The use of photodegradation becomes an increasingly popular method for treating water. In this study, the photodegradation of Reactive Red 66, Reactive Red 120 dyes and textile wastewater was studied under UV and visible light. To enhance the photoresponse of the Iron (II, III) oxide, modifications were made to the graphene oxide. Iron (II, III) oxide and its nanocomposite photocatalysts were subject to characterization techniques; including FT-IR, Raman, XRD, DRS, zeta potential VSM, SEM, EDAX, and AFM. A series of experiments were conducted to optimize several parameters in the photodegradation process. Under optimal conditions, the removal efficiency of Reactive Red 66 and Reactive Red 120 dyes using Iron (II, III) oxide was found to be 94.8, and 88.5%, respectively. Also, removal percentage of these dyes using Iron (II, III) oxide/GO nanocomposite has been 95.2, and 91.3%. After three days of exposure to visible light, the removal percentage of Reactive Red 66 using Iron (II, III) oxide and Iron (II, III) oxide/GO was 85.7 and 92.1%, respectively. Similarly, the percentage of Reactive Red 120 removal using Iron (II, III) oxide and Iron (II, III) oxide/GO under visible light after three days were 81.9 and 85.0%, respectively. The dye removal efficiency was determined in textile wastewater by measuring BOD and COD. Kinetic studies demonstrated that the photocatalytic reactions followed the pseudo-second-order. Additionally, the reusability of the prepared photocatalyst was also evaluated.

Keywords Iron (II, III) oxide nanoparticles · Graphene oxide matrix · Photodegradation · Organic dye pollutants · Textile wastewater

Introduction

Various industries rely heavily on synthetic dyes, including printing, textiles, and painting. Unfortunately, the release of these dyes into water effluents poses a major health risk globally, impacting both the environment and human health (Lellis et al. 2019). Of particular concern are textile dyes, as they often consist of organic compounds (Benkhaya et al. 2020). In addition, synthetic dyes are typically non-biodegradable, creating a significant risk to human health (Al-Tohamy et al. 2022). In recent years, many techniques

have been explored to eliminate from wastewater, including adsorption, irradiation, chemical oxidation, coagulation, electrochemical procedures, membrane routes, and biological processes (Samsami et al. 2020; Naik et al. 2021; Theerthagiri et al. 2021, 2022; Li et al. 2021). Among these approaches, adsorption and degradation has emerged as a promising strategy for remediating synthetic dye removal from wastewater due to its wide range of applications and ability to operate under various conditions (Dutta et al. 2021). Iron-based oxides, in particular, have garnered significant attention in research due to their exceptional properties, including reusability, non-toxicity, high adsorption capacity, long-term stability, affordability, and ease of removal from solution without producing secondary pollution. Iron particles are remarkably effective for treating wastewater, owing to their inherent magnetism, which allows for the use of a magnetic field to extract contaminants from wastewater (Kim and Choi 2017; Aragaw et al. 2021). Additionally,

✉ Shabnam Sheshmani
shabnam_sheshmani@yahoo.com

¹ Department of Chemistry, College of Basic Sciences, Yadegar-E-Imam Khomeini (RAH) Shahre Rey Branch, Islamic Azad University, Tehran, Iran

anionic organic dyes containing π - π aromatic bonds, sulfite, and amino groups can form weak interactions with the surface of iron particles (Goswami et al. 2023).

Alternatively, synthesizing magnetic photocatalyst nanoparticles has been a growing area of interest in recent years. This can be achieved through a variety of methods, including co-precipitation, hydrothermal, sol-gel, sonochemical, microwave, and emulsion techniques (Díez et al. 2022; Park et al. 2018). Iron (II, III) oxide and its composite nanoparticles have demonstrated their effectiveness as photocatalysts for various molecules, including Methylene Blue, Methyl Red, Congo Red, Methylene Orange, Levofloxacin, Rhodamine B, Malachite Green, and Cr(VI) (Villegas et al. 2020; Tung and Daoud 2009; Solomon et al. 2012; Mangrulkar et al. 2012; Kumar et al. 2016; Hu et al. 2011; [https://doi.org/10.4028, www.scientific.net, MSF.688.376](https://doi.org/10.4028/www.scientific.net/MSF.688.376); Rabhani et al. 2015; Hosseinian et al. 2011; Reza et al. 2016; Giri and Das 2016; Mishra et al. 2016). The use of the UV/nano-Iron (II, III) oxide system can enhance the photodegradation efficiency of the organic pollutants due to the transfer of photo-generated electrons. This process results in the separation of electrons and holes. The holes act as strong oxidants, which can oxidize OH^- and H_2O molecules adsorbed on the Iron (II, III) oxide surface, generating HO^\bullet free radicals. These radicals, in turn, are adsorbed onto the Iron (II, III) oxide surface, where they act as strong oxidants that not only oxidize the adsorbed organic compounds but also diffuse into the bulk solution to oxidize other organic compounds. Following a sequence of oxidative processes, the organic compound can ultimately be transformed into harmless products such as CO_2 , H_2O , and NH_3 (Bibi et al. 2021; Afari et al. 2023; Sheshmani and Nayeibi 2019). The availability of visible light as an energy source opens up opportunities for utilizing natural sunlight, which is abundant and environmentally friendly. This characteristic makes visible light photocatalysis particularly appealing for applications such as environmental remediation, water purification and air pollution control.

Chemical modification of iron oxide using graphene oxide has been found to increase its photocatalytic properties (Sheshmani et al. 2017; Li et al. 2013; Suresh et al. 2018). Iron (II, III) oxide/graphene oxide exhibits photocatalytic activity due to a combination of factors, such as its high surface area and unique electronic properties. Graphene oxide provides a large surface area for adsorption of organic pollutants, while Iron (II, III) oxide nanoparticles act as electron acceptors to facilitate photocatalytic reactions. Several studies have demonstrated the photocatalytic activity of Iron (II, III) oxide/graphene oxide for the degradation of various organic pollutants, including dyes and pharmaceuticals. For example, Iron (II, III) oxide/graphene oxide nanocomposites have been shown to effectively degrade dyes such as Rhodamine B

and Methylene Blue under visible light. In addition, Iron (II, III) oxide-graphene oxide has been demonstrated to be effective in the degradation of pharmaceuticals (Sheshmani 2013; Vinodhkumar et al. 2020; Pervez et al. 2020; Jiao et al. 2015; Wang et al. 2018). Overall, the photocatalytic properties of Iron (II, III) oxide-graphene oxide make it a promising material for the development of advanced water treatment technologies and other environmental applications.

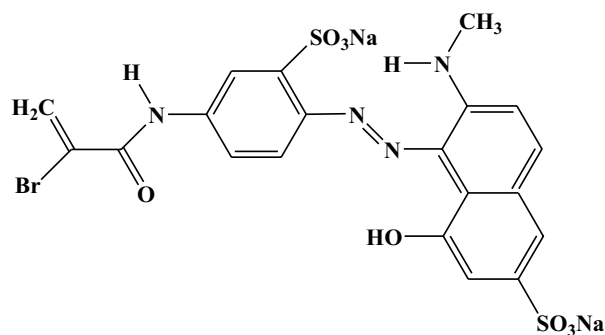
To date, there have been limited scientific studies on the use of proposed magnetic nanocomposites for degradation of Reactive Red 66 (R66) and Reactive Red 120 (R120) dyes. The objective of this research is to create magnetic oxide nanoparticles and Iron (II, III) oxide/graphene oxide composite that can effectively eliminate R66 and R120 from aqueous solutions. This research offers a comprehensive exploration of the preparation of composite, along with morphological and crystallographic characterizations, as well as kinetics, with the sole aim of demonstrating the potential application of magnetic nanocomposite. The Iron (II, III) oxide and Iron (II, III) oxide/GO composites produced in this study have several advantages, such as low cost, high removal capacity, and effortless regeneration using only a magnet, which eliminates the need for additional steps to separate the adsorbent. Consequently, the materials investigated here exhibit environmentally friendly photocatalyst properties and provide an alternative solution for addressing wastewater issues.

Materials and methods

Materials

This study employed ferric chloride (FeCl_3) with a purity of 98% from Merck, ferrous chloride tetrahydrate ($\text{FeCl}_2 \cdot 4\text{H}_2\text{O}$) with a purity of 98% from Merck, and aqueous ammonia ($\text{NH}_3(\text{aq})$) with a concentration of 25% and a purity of 99.99% from Merck. Also, Sigma-Aldrich provided commercial graphite flakes with a particle size of 150 mesh and a purity of 99.5%. Reactive Red 66 (R66) and Reactive Red 120 (R120) dyes were procured from Nordex International and D.Z.E Dye Company in the UK. Reactive Red 66 is a monoazo reactive dye that has a molecular formula of $\text{C}_{20}\text{H}_{15}\text{BrN}_4\text{Na}_2\text{O}_8\text{S}_2$, a molecular weight of 629.37 gmol^{-1} , and a CAS registry number of 12,226-33-4. Reactive Red 120 is a diazo reactive dye that has a molecular formula of $\text{C}_{44}\text{H}_{24}\text{Cl}_2\text{N}_{14}\text{Na}_6\text{O}_{20}\text{S}_6$, a molecular weight of $1469.98 \text{ gmol}^{-1}$, and a CAS registry number of 61,951-82-4. These reactive dyes are commonly utilized in the textile industry, and their chemical structures are illustrated in Fig. 1.

a)



b)

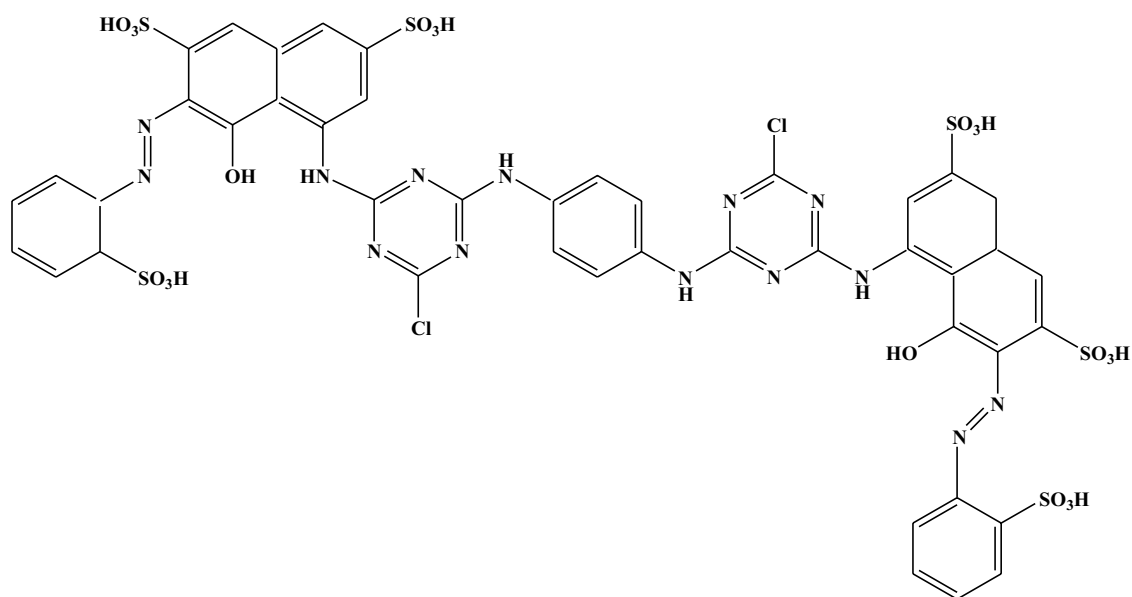


Fig. 1 The chemical structures of **a** R66 and **b** R120 dyes

Characterization techniques

Thermo AVATAR equipment was employed to carry out Fourier transform infrared spectroscopy (FT-IR) measurements over the $500\text{--}4000\text{ cm}^{-1}$ range. This technique can provide information about the chemical composition. Around 10 mg of the samples were blended with KBr to produce a transparent pill for FT-IR measurements. A Raman Takram, P50C0R10 TEKSAN apparatus was utilized to determine the vibrational modes, with an excitation source of 532 nm and laser power varying from 0.5–70 mW. The spectra were within the $100\text{--}200\text{ cm}^{-1}$ range. A PHILIPS PW1730 with Cu $K\alpha$ radiation was applied to measure Powder X-ray diffraction (XRD) patterns, and the intensity data was gathered over a 2θ range

from 10 to 80° . The Joint Committee of Powder Diffraction Standard (JCPDS) database files were used to index the patterns.

Zeta potential measurements were conducted using a Zeta Horiba instrument, Zeta-DIs Zetasizer, Malvern, Cambridge, UK. The samples were loaded into vials for the zeta potential analyses. This technique was used to measure the surface charge of particles in a suspension. By determining the magnitude and sign of the zeta potential, this method can provide information about the stability of the suspension and its potential for interacting with other surfaces or dyes. The magnetic properties of the samples were studied by measuring magnetic hysteresis loops using a vibrating sample magnetometer (VSM) in the LBKFB 1.4 T equipment. VSM analysis involves placing a small sample of the material in

a magnetic field and measuring the resulting magnetization while varying the strength of the field. Diffuse reflectance spectroscopy, DRS S-4100 SCINCO, was applied to determine the optical properties of a material in the ultraviolet, visible, and near-infrared regions of the electromagnetic spectrum. The intensity and wavelength of the scattered light can provide information about the electronic structure of the material, including band gap energy.

The FEG electron microscope, the TESCAN MIRA III model, examined the morphology and particle size in scanning electron microscope (SEM) mode. To obtain optimal resolution, all samples were gold-sputtered. The SEM unit was equipped with an Energy Dispersive Spectroscopy (EDS) system. EDX analysis can provide in-depth information about the composition of samples at the microscopic level. Information about surface properties, including topography and roughness, was provided by atomic force microscopy, the AFM Veeco model.

Preparation of the Iron (II, III) oxide and nanocomposite

A co-precipitation method was employed to prepare the magnetic Iron (II, III) oxide nanoparticles, ferric chloride (FeCl_3), ferrous chloride tetrahydrate ($\text{FeCl}_2 \cdot 4\text{H}_2\text{O}$), and aqueous ammonia ($\text{NH}_3(\text{aq})$) were utilized as starting materials. Fe^{3+} and Fe^{2+} were employed as iron precursors in a 2:1 molar ratio, and each was dissolved in 15 mL of distilled water. Aqueous ammonia was added to the iron solution until the pH reached 12, and stirring was carried out for one hour under a N_2 gas atmosphere at room temperature.

The GO was prepared using the Staudenmaier method (Chen et al. 2020). Initially, sulfuric acid (18 mL) and nitric acid (9 mL) were cooled in an ice bath. Next, graphite powder (1 g) was added with stirring until well dispersed. Slowly, potassium chlorate (11 g) was added over a one-hour period. An increase in temperature should be avoided. The mixture was stirred for 4 days at room temperature. Once the reaction was complete, the mixture was filtered and poured into 100 mL of deionized water. The product was then washed with deionized water until the pH was 6, after which it was vacuum-dried.

Iron (II, III) oxide-based graphene oxide was prepared by adding Iron (II, III) oxide (0.2 g) into 20 mL of distilled water to graphene oxide (0.5 g) in an ultrasound bath. The mixture was stirred for 4 h and then washed thoroughly with distilled water before being dried at 60 °C for one hour.

Degradation studies

The effectiveness of magnetic nanocomposites in degrading R66 and R120 dyes was evaluated through batch photodegradation experiments. The experiments were performed

using a 25 mL solution containing the dyes at a concentration of 20 mgL^{-1} and at a temperature of 25 °C (Afari et al. 2023; Sheshmani and Nayebi 2019). Magnetic nanocomposites (0.05 g) were added to the solution and vigorously stirred at 150 rpm for 30 min at pH values ranging from 2 to 9 to ensure extensive dye removal. The mixture was then separated, and the dye concentration was measured using UV–Vis spectroscopy with a Cary 60 instrument from Agilent Technologies (USA). Each adsorption experiment was repeated twice to compare the adsorption behavior of R66 and R120 dyes and Iron (II, III) oxide and Iron (II, III) oxide/GO composites.

Results and discussions

Structure determination by FT-IR, Raman, zeta potential, and XRD

The co-precipitation of the aqueous solution containing FeCl_3 and $\text{FeCl}_2 \cdot 4\text{H}_2\text{O}$ in a basic medium results in the formation of iron(III) hydroxide ($\text{Fe}(\text{OH})_3$) and oxyhydroxide ($\alpha\text{-FeOOH}$). Subsequently, the oxyhydroxide nucleate can be converted into Iron (II, III) oxide.

The FT-IR spectra of the Iron (II, III) oxide nanoparticles are depicted in Fig. 2. The bands observed at 440 and 588 cm^{-1} were attributed to Fe–O bond vibrations, which are associated with the tetrahedral and octahedral sites of Iron (II, III) oxide. The spectra also revealed the stretching and bending of O–H groups from water molecules at 3417 and 1617 cm^{-1} , respectively. Also, the presence of Iron (II, III) oxide nanoparticles with O–H hydroxyl bonds on unsaturated surface Fe atoms at the same positions is mentioned above. The FT-IR analysis of Iron (II, III) oxide/GO nanocomposite revealed several characteristic peaks. The broad absorption band at 3390 cm^{-1} corresponds to the stretching vibration of O–H groups from moisture and adsorbed water molecules. The peak observed at 1733 cm^{-1} is attributed to the stretching vibration of the carbonyl group (C=O) of carboxylic acid groups in graphene oxide, while the peak at 1624 cm^{-1} is due to the stretching vibration of the C=C bond in graphene oxide. The Fe–O bond vibration in Iron (II, III) oxide is represented by the peak observed at 440 and 577 cm^{-1} . These peaks confirm the presence of both Iron (II, III) oxide and graphene oxide in the nanocomposite (Fig. 2).

Several characteristic peaks are observed in the Raman spectrum of GO, including the D, G, 2D, D', and D + G peaks. The D peak (around 1350 cm^{-1}) represents the breathing mode of sp^2 carbon atoms, often associated with defects and disorder in the graphene lattice. The G peak (around 1580 cm^{-1}) corresponds to the E_{2g} mode of sp^2 -bonded carbon atoms and indicates GO's graphitic structure. The 2D peak (around 2700 cm^{-1}) is a second-order

Fig. 2 FT-IR spectra of Iron (II, III) oxide and Iron (II, III) oxide/GO

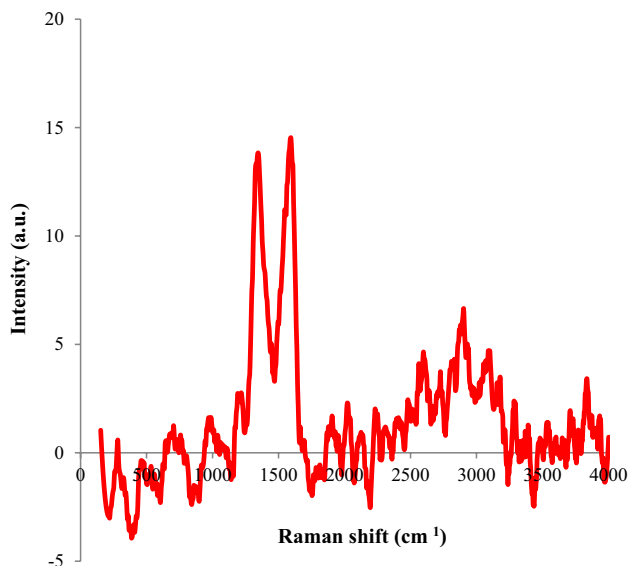
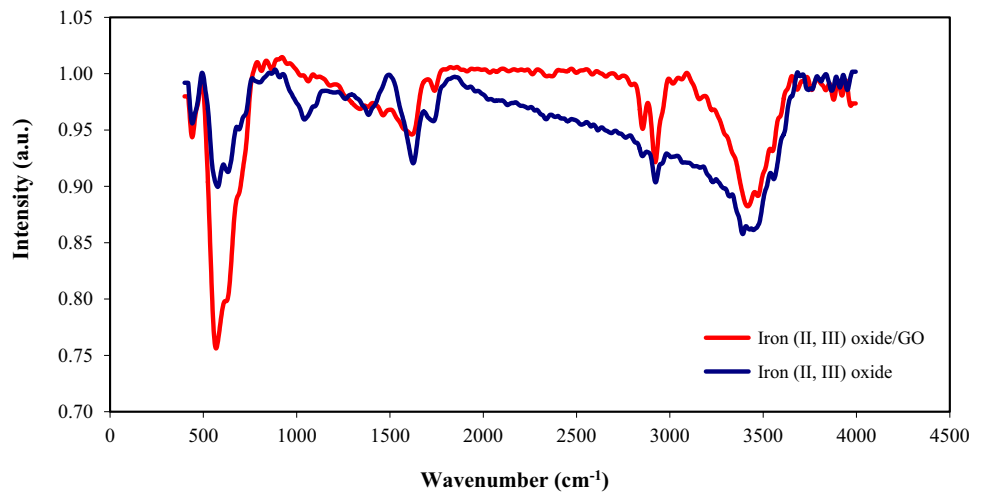


Fig. 3 Raman spectra of Iron (II, III) oxide/GO nanocomposite

scattering process of the G peak and is a sensitive indicator of the number of graphene layers and the degree of stacking. In addition to these three main peaks, other peaks may also be observed in the Raman spectrum of GO, such as the D' (around 1620 cm^{-1}) peak and the D+G peak (around 2930 cm^{-1}). The Raman spectra of Iron (II, III) oxide presented two characteristic peaks observed at around 669 and 485 cm^{-1} , corresponding to the A_{1g} and E_g modes of Iron (II, III) oxide, respectively. These peaks are attributed to the symmetric stretching and bending vibrations of the oxygen ions, respectively (Poh et al. 2012). The presence of these two peaks confirms the successful synthesis of Iron (II, III) oxide. Figure 3 displays the Raman spectra of Iron (II, III) oxide/GO, showing characteristic peaks at approximately 1329 and 1583 cm^{-1} , corresponding to the D and

G bands of graphene oxide, respectively (Shebanova and Lazor 2003). Additionally, peaks are observed at around 687 and 446 cm^{-1} , indicating the presence of the A_{1g} and E_g modes of Iron (II, III) oxide, respectively, in the graphene oxide matrix. These peaks provide evidence for the successful synthesis of Iron (II, III) oxide-graphene oxide. The position and intensity of these peaks can provide valuable information about the level of oxidation, functionalization, and structural defects present in the Iron (II, III) oxide/GO.

Several factors, such as the pH of the solution, the size and shape of the particles, and the presence of surface coatings or functionalization, can influence the zeta potential of Iron (II, III) oxide and Iron (II, III) oxide/GO. As a result, the zeta potential of Iron (II, III) oxide is not a fixed value and can vary depending on the specific conditions of the system. Iron (II, III) oxide nanoparticles typically exhibit a negative surface charge owing to the presence of hydroxyl and/or oxygen groups on their surface. Therefore, the overall surface charge of the Iron (II, III) oxide-graphene oxide composite will depend on the concentration and distribution of the two components. The magnitude of the zeta potential varies between -10 and -100 mV , depending on the specific conditions of the system (Fig. 4).

The XRD diffraction pattern of Iron (II, III) oxide is presented in Fig. 5, with the primary diffraction planes observed at $2\theta = 30.1, 35.5, 43.0, 53.2, 57.1,$ and 62.7° , which correspond to the (220), (311), (400), (422), (511), and (440) planes, respectively. These peaks were identified and indexed to the standard pattern of magnetite with JCPDS 98–011–128. The Iron (II, III) oxide/GO nanocomposite's XRD pattern is presented in Fig. 5. The observed diffraction peaks at 2θ values of $30.2, 35.6, 43.1, 53.4, 57.2,$ and 62.8° correspond to the (220), (311), (400), (422), (511), and (440) planes, respectively, of Iron (II, III) oxide. Additionally, the peak at 10.5° corresponds to the (002) plane of graphene oxide, indicating the presence of both Iron (II, III) oxide and

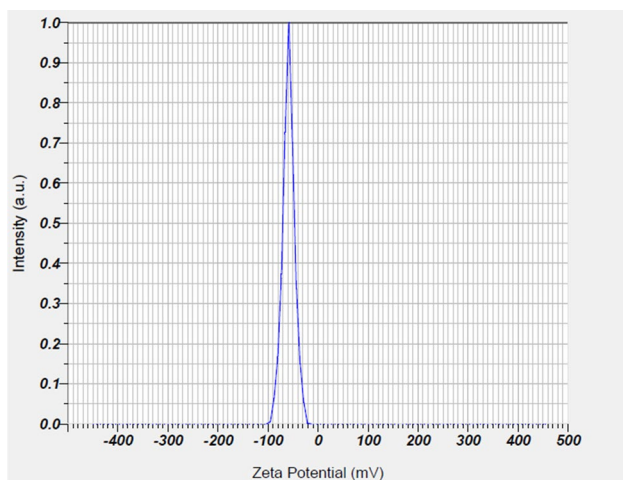


Fig. 4 Zeta potential of Iron (II, III) oxide/GO nanocomposite

GO in the nanocomposite. These characteristic peaks serve as evidence for the presence of both Iron (II, III) oxide and GO in the prepared nanocomposite.

Studies on optical and magnetic properties

The ultraviolet differential reflectance spectroscopy (UV-DRS) method was used to study the band gap measurements and optical properties of Iron (II, III) oxide and Iron (II, III) oxide/GO. The absorption peak and band gaps for each material are shown in Fig. 6.

The magnetic properties were analyzed using a Vibrating Sample Magnetometer (VSM). Magnetic hysteresis loops (MS) were measured at room temperature, as shown in Fig. 7. The Iron (II, III) oxide sample has a magnetic moment of approximately 55 emu/g, which is significantly higher than the value of 12.5 emu/g observed for Iron (II, III) oxide/GO. The presence of graphene oxide can lead to changes in the magnetic property of the Iron (II, III) oxide/

GO compared to Iron (II, III) oxide alone. This point indicates the decoration of Iron (II, III) oxide particles on graphene oxide.

Studies on morphological aspects

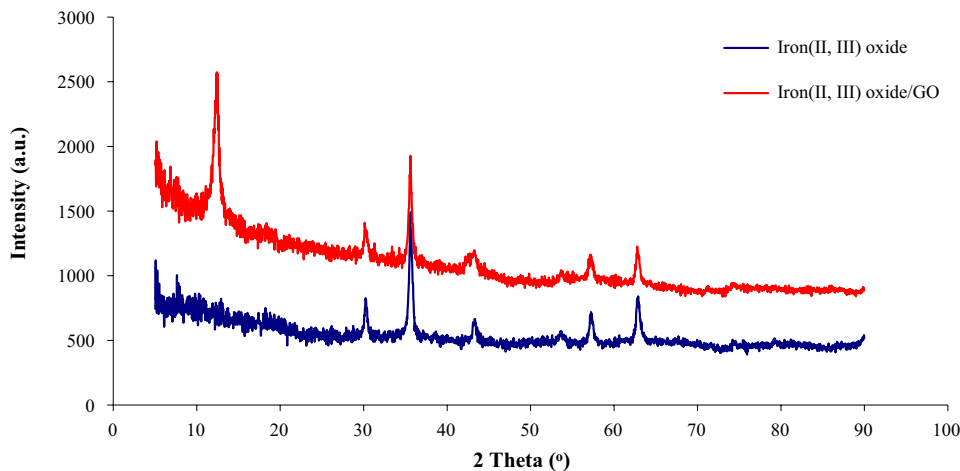
SEM–EDS analyses were performed to investigate the solid's morphology and composition. The SEM images of the Iron (II, III) oxide sample showed particles with a spherical shape (about 20 nm in particle size) and rough surface morphology (Wang et al. 2013). Additionally, the EDS elemental analysis revealed that the sample was composed of 67% Fe and 33% O (Table 1). SEM images and atom mapping are shown in Fig. 8.

Figure 9 displays SEM images of graphene oxide, which typically reveal sheets with wrinkles and folds. The thickness of these sheets can vary from 14–24 nm. The GO sheets' wrinkled and folded structures are attributed to the presence of oxygen-containing functional groups that disrupt the sp^2 carbon network of graphene and introduce defects into the structure.

The SEM images of Iron (II, III) oxide/GO exhibited similar morphologies to those of the Iron (II, III) oxide sample, with spherical particles decorating the graphene oxide sheets. However, some particles tended to agglomerate, as shown in Fig. 10. The EDS analysis confirmed that the sample had a composition of 14.08% Fe, 39.77% O, and 46.15% C, indicating successful incorporation of iron into the structure (Table 2). Figure 11 shows the atom mapping of Iron (II, III) oxide/GO as well as the EDS analysis. The presence of both Fe species and graphene sheets in the composite is consistent with FT-IR, XRD, and Raman analysis.

AFM imaging can reveal the topography of Iron (II, III) oxide/GO, along with the size and distribution of the nanoparticles within the graphene oxide matrix. Typically, AFM images of Iron (II, III) oxide/GO exhibit a mostly flat surface with occasional bumps or features corresponding

Fig. 5 XRD pattern of Iron (II, III) oxide and Iron (II, III) oxide/GO



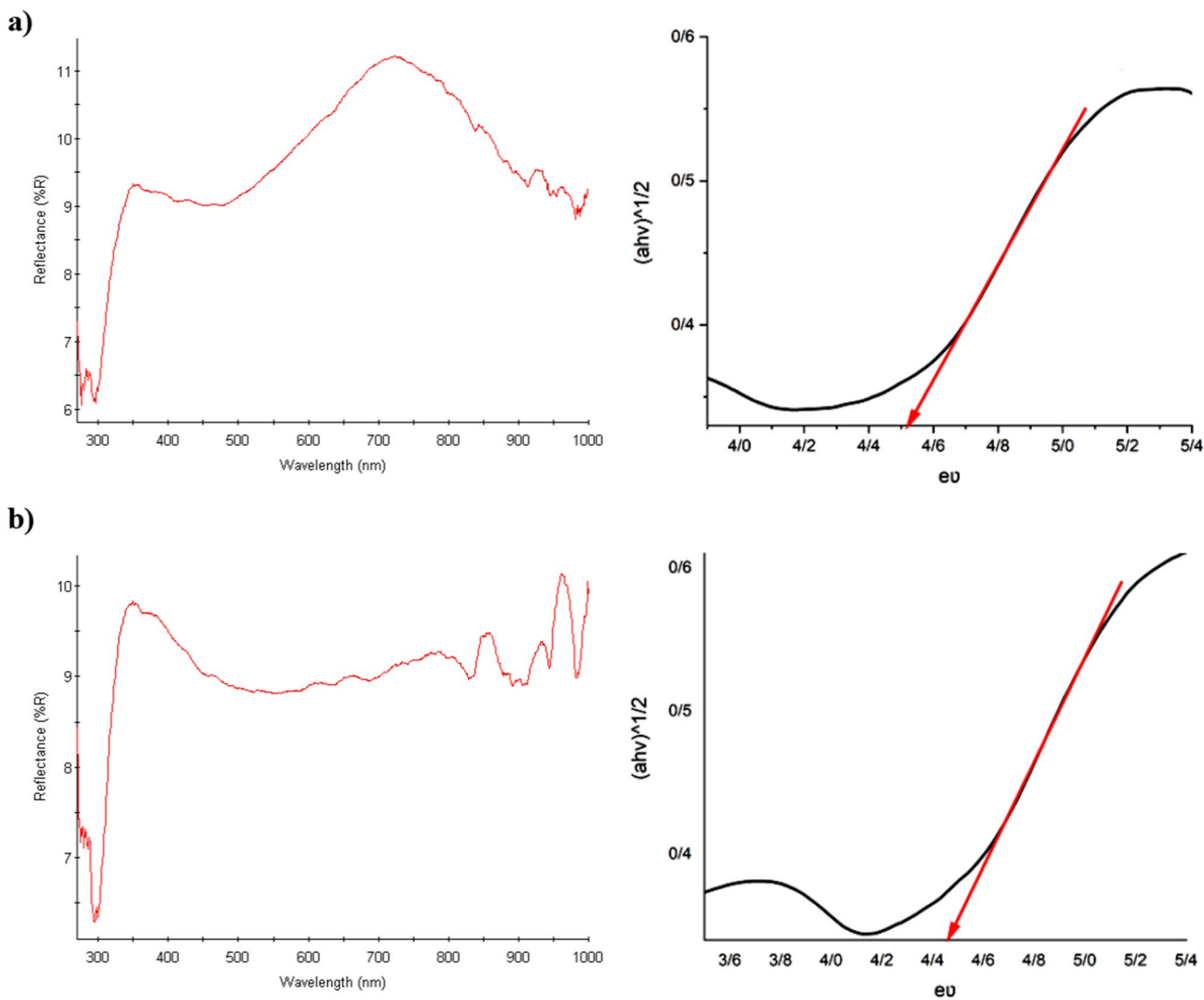


Fig. 6 UV-DRS adsorption peaks and band gap values of a Iron (II, III) oxide and b Iron (II, III) oxide/GO

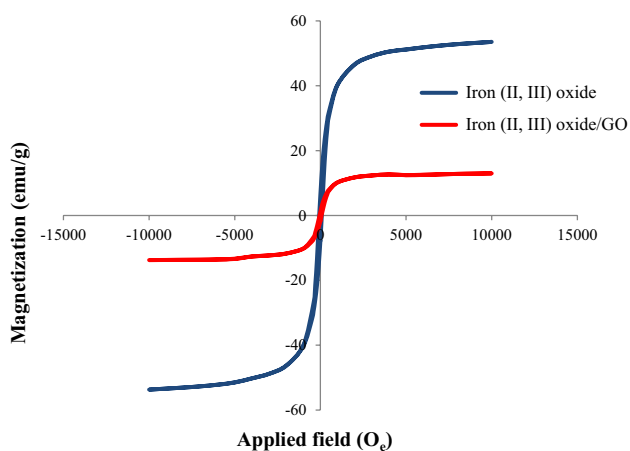


Fig. 7 VSM analysis of Iron (II, III) oxide and Iron (II, III) oxide/GO

to the nanoparticles. Additionally, the height distribution of surface features can be represented by a histogram generated from the AFM data (Fig. 12).

Analyzing the AFM images makes it possible to quantify various surface parameters, such as surface topography, roughness, and the size and distribution of surface features. Statistical parameters such as RMS roughness or Ave roughness can be used to measure the roughness of a surface, while parameters such as Median Ht can be used to measure the size and distribution of nanoparticles or other surface features (Table 3).

$R_p(v)$ refers to the radius of curvature as a function of the vertical position (v) of the cantilever. Rms rough is the root mean square height of the surface features or roughness on a sample. Ave roughness is assigned to the average height of the surface features or roughness on a sample.

Table 1 Energy dispersive X-ray spectroscopy (EDAX) analyses of Iron (II, III) oxide

Elt	Line	Int	K	Kr	W%	A%	ZAF	Pk/Bg	LConf	HConf
O	Ka	345.3	0.2827	0.2416	33.00	63.23	0.7321	28.80	32.35	33.65
Fe	Ka	504.0	0.7173	0.6130	67.00	36.77	0.9149	33.25	65.91	68.09
			1.0000	0.8546	100.00	100.00				

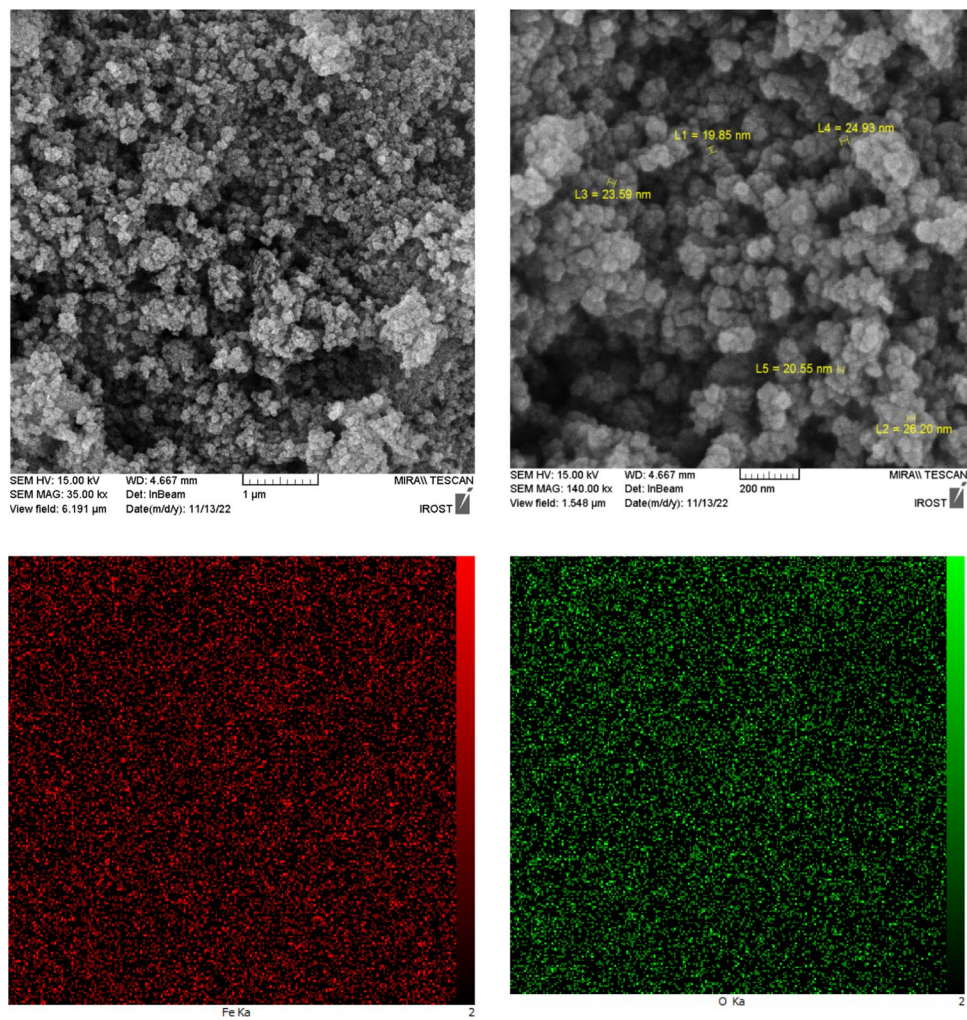
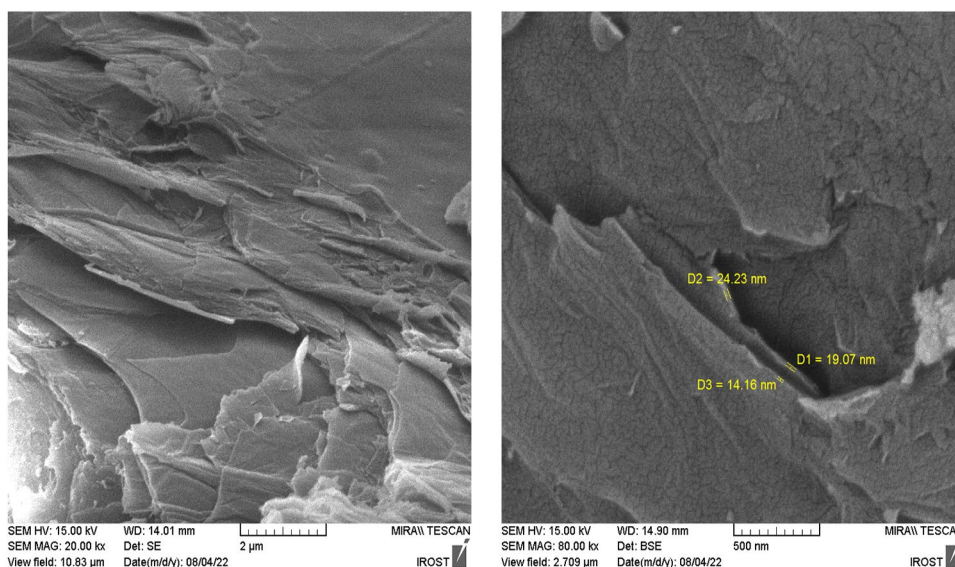
Fig. 8 SEM images, atom mapping of Iron (II, III) oxide, and EDS analysis

Fig. 9 SEM images of GO

Median Ht refers to the median height of the surface features or roughness on a sample.

Dye removal studies

Dye removal studies using Iron (II, III) oxide

This study investigated the effect of initial pH, photocatalyst dosage, dye concentration, and contact time on the degradation of R66 and R120 dyes using Iron (II, III) oxide and Iron (II, III) oxide/GO as photocatalysts. Dye removal experiments were conducted by varying the initial pH from 2 to 9, with a constant initial dye concentration of 20 mg/L, Iron (II, III) oxide dosage of 0.05 g, and a UV irradiation time of 30 min. The results presented in Fig. 13 indicate that high pH values (alkaline conditions) led to a decrease in the photodegradation percentage of R66 and R120 dyes. Under acidic conditions, an abundance of H^+ ions leads to an increase in the surface charge of the photocatalyst (Ashori et al. 2016; Aghabozorg et al. 2006; Soleimannejad et al. 2005). The maximum uptake values of R66 and R120 were achieved at pH = 2 using Iron (II, III) oxide, with values of 82% and 61.96%, respectively. These findings emphasize the importance of controlling the pH when using Iron (II, III) oxide nanoparticles for dye degradation. The effect of Iron (II, III) oxide dosage (ranging from 0.05 to 0.09 g) on the photodegradation of R66 and R120 was also investigated, with results indicating that an increase in the photocatalyst dosage led to a corresponding increase in the degradation percentage. Specifically, at a dose of 0.08 g Iron (II, III) oxide, degradation percentages of 87.63% and 60.07% were observed for R66 and R120 dye removal, respectively (Fig. 13).

These results suggest that the dye molecules are rapidly absorbed during the initial stage, with further occupation of the sites occurring as the reaction progresses. This, in turn, leads to a decrease in the interactions between the photocatalyst and the azo dye. Therefore, the findings suggest that excess photocatalysts can lead to active site saturation. The dye concentration in a solution is a critical factor affecting the efficiency of dye removal. Typically, higher dye concentrations make it more challenging to remove the dye from the solution. This is because there are more dye molecules per unit volume at higher concentrations, which can lead to saturation of the photocatalyst sites and a decrease in the available surface area for dye removal. In this study, an initial concentration of 30 mg/L increased the removal percentage of R66 to 85.1%. In comparison, for an initial dye concentration of 20 mg/L, the removal percentage of R120 was 68.1% (Fig. 13). The contact time between the dye solution and the adsorbent material is an important factor affecting dye removal efficiency. During the adsorption process, dye molecules transfer from the solution to the surface of the composite. At the beginning of the photodegradation process, the concentration gradient between the solution and the photocatalyst surface is high, resulting in a rapid dye removal rate. As the adsorption-photodegradation progresses, the concentration gradient decreases, and the rate of adsorption slows down until equilibrium is reached. In this study, the maximum removal of Red 66 (91.84%) was achieved after 90 min of contact time, while the maximum removal of R120 (83.22%) was achieved after 75 min of contact time (Fig. 13).

Fig. 10 SEM images of Iron (II, III) oxide/GO

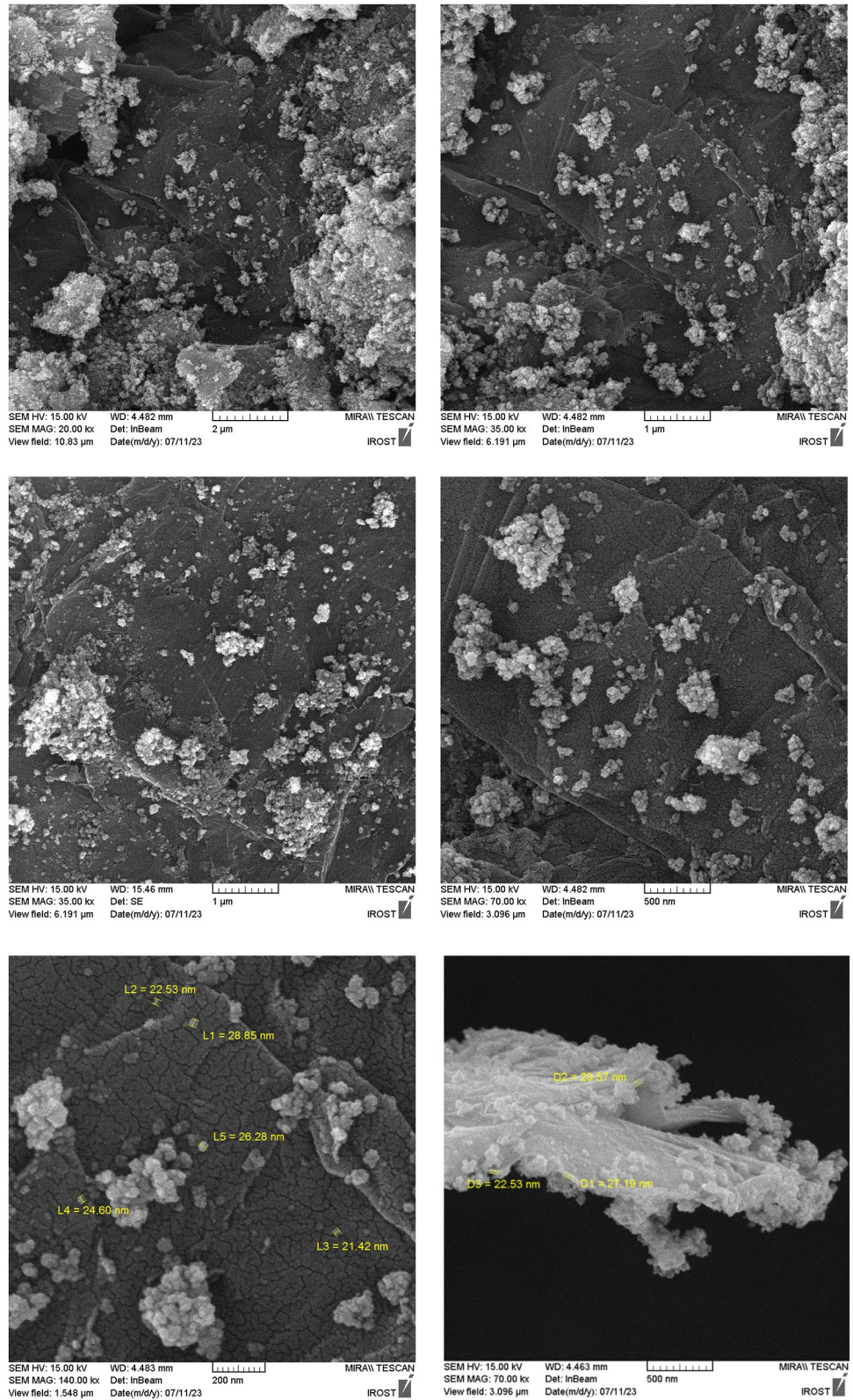


Table 2 Energy dispersive X-ray spectroscopy (EDAX) analyses of Iron (II, III) oxide/GO

Elt	Line	Int	K	Kr	W%	A%	ZAF	Pk/Bg	LConf	HConf
C	Ka	110.3	0.5172	0.2393	46.15	58.39	0.5185	77.91	44.54	47.75
O	Ka	105.0	0.2453	0.1135	39.77	37.78	0.2853	49.96	38.36	41.19
Fe	Ka	58.5	0.2375	0.1099	14.08	3.83	0.7804	12.58	13.41	14.75
			1.0000	0.4627	100.00	100.00				

Dye removal studies using Iron (II, III) oxide/GO

Figure 14 provides information on the impact of various factors, such as pH (2–9), Iron (II, III) oxide/GO dosage (0.03–0.09 g), dye concentration (5–50 mg/L), and contact time (10–90 min), on the removal of dye. This figure shows that alkaline conditions reduced the photodegradation of R66 and R120 dyes. Iron (II, III) oxide/GO achieved the highest uptake values for R66 and R120 at pH=2, reaching 88.4, and 70.2%, respectively. Also, the highest degradation percentages were achieved using 0.04 and 0.05 g Iron (II, III) oxide/GO, resulting in 92 and 90% removal for R66 and R120, respectively. According to the results presented in Fig. 14, the removal percentage of R66 and R120 increased to 95.26 and 89.37% at an initial concentration of 20 mg/L. The figure shows that the highest removal of Red 66 (93.57%) occurred after 60 min of contact time, while the maximum removal of R120 (91.38%) was achieved after 75 min.

Continuing the experiment, the dye removal percentages were measured using Iron (II, III) oxide and Iron (II, III) oxide/GO under UV and Visible light irradiations, as illustrated in Fig. 15. The data comparison revealed that the presence of Iron (II, III) oxide on the GO surface enhanced the photodegradation process.

Dye removal kinetic

Adsorption efficiency can be assessed using kinetic models, such as the pseudo-first-order and pseudo-second-order equations. The first-order kinetic model is frequently employed to describe dye adsorption, and Eq. 1 represents this model:

$$\ln(q_e - q_t) = \ln q_e - k_1 t \quad (1)$$

where q_e and q_t refer to the adsorption capacity at equilibrium and at different times, respectively, and the rate constant of the adsorption process's pseudo-first-order model is denoted by k_1 (min^{-1}).

The pseudo-second-order model identifies chemisorption as the rate-limiting step, while adsorption can take place at

sites where no interactions between the adsorbates occur. The equation representing this model is expressed in Eq. 2:

$$t/q_t = 1/k_2 q_{eq}^2 + t/q_{eq} \quad (2)$$

where k_2 ($\text{g} \cdot \text{mg}^{-1} \cdot \text{min}^{-1}$) is the rate constant of pseudo-second-order adsorption.

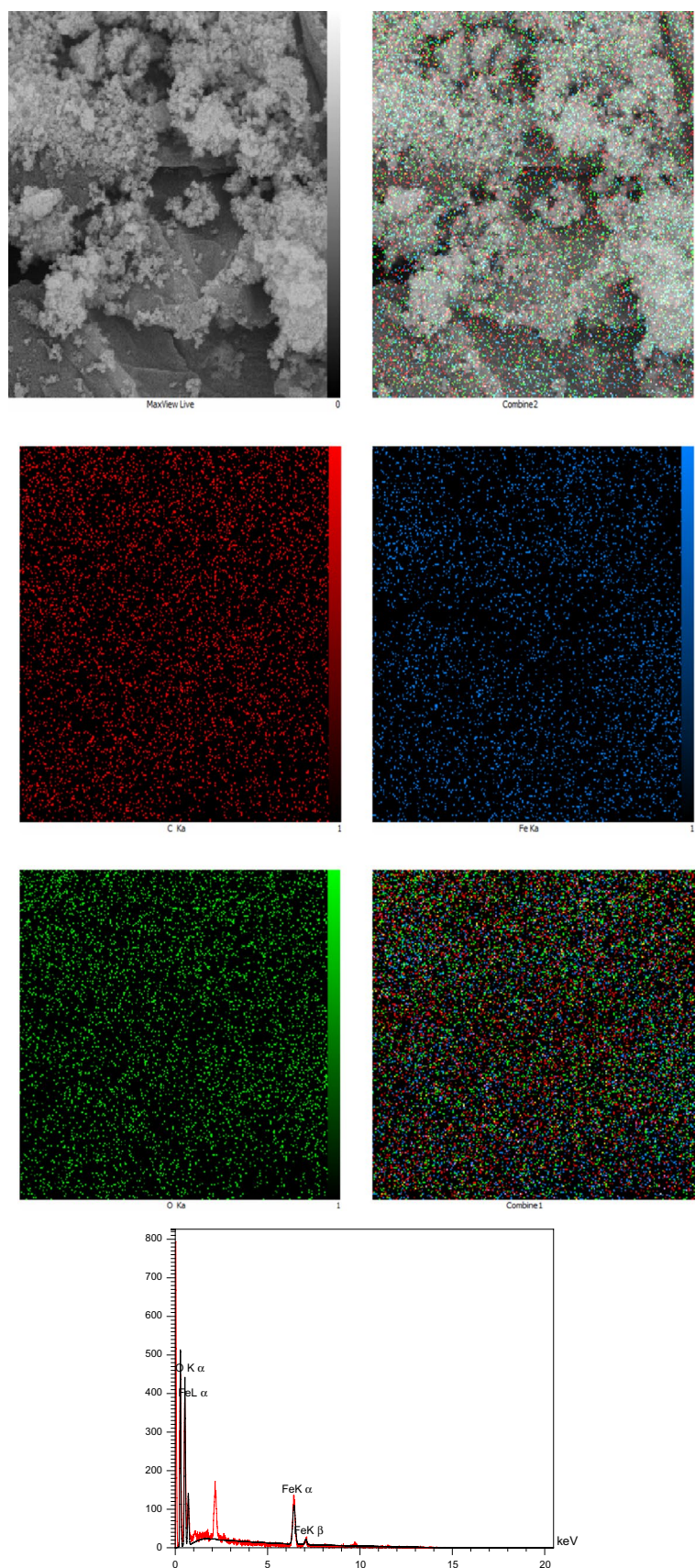
The parameters obtained from the pseudo-first-order model have R^2 values of 0.873 and 0.840 using Iron (II, III) oxide on Red 66 and Red 120 removal. On the other hand, the R^2 values for the second-order kinetic model using Iron (II, III) oxide are 0.952 and 0.999 (Fig. 16). The pseudo-first-order model yielded parameters with R^2 values of 0.56 and 0.93 for the removal of Red 66 and Red 120, respectively, using Iron (II, III) oxide/GO. In contrast, the second-order kinetic model using Iron (II, III) oxide/GO produced R^2 values of 0.99 and 0.99, as shown in Fig. 17. These results suggest that the pseudo-first-order model is not highly accurate. Therefore, the most optimal outcomes are achieved using the pseudo-second-order.

The identification of a pseudo-second-order kinetic model in photocatalytic reactions holds practical implications for the design and optimization of photocatalytic processes. This model implies that the rate of the photocatalytic reaction is primarily determined by the concentration of both the reactants and the catalyst surface sites available for adsorption. Practically, this insight allows researchers and engineers to better understand and control the reaction kinetics in photocatalytic systems. By manipulating the reactant concentrations and the surface area or loading of the photocatalyst, it becomes possible to enhance the reaction rate and improve the overall efficiency of the process.

Dye removal from textile wastewater

To eliminate any suspended particles, the textile wastewater was filtered through 0.45 mm mesh filter paper, and the resulting solution was treated with a photocatalytic reaction under optimal conditions. The reaction successfully resulted in a colorless solution. To determine the initial and final concentrations, a standard solution was prepared by mixing R66 and textile wastewater. Five volumetric flasks (50 mL) were filled with the clear wastewater solution (25 mL), and

Fig. 11 Atom mapping of Iron (II, III) oxide/GO and EDS analysis



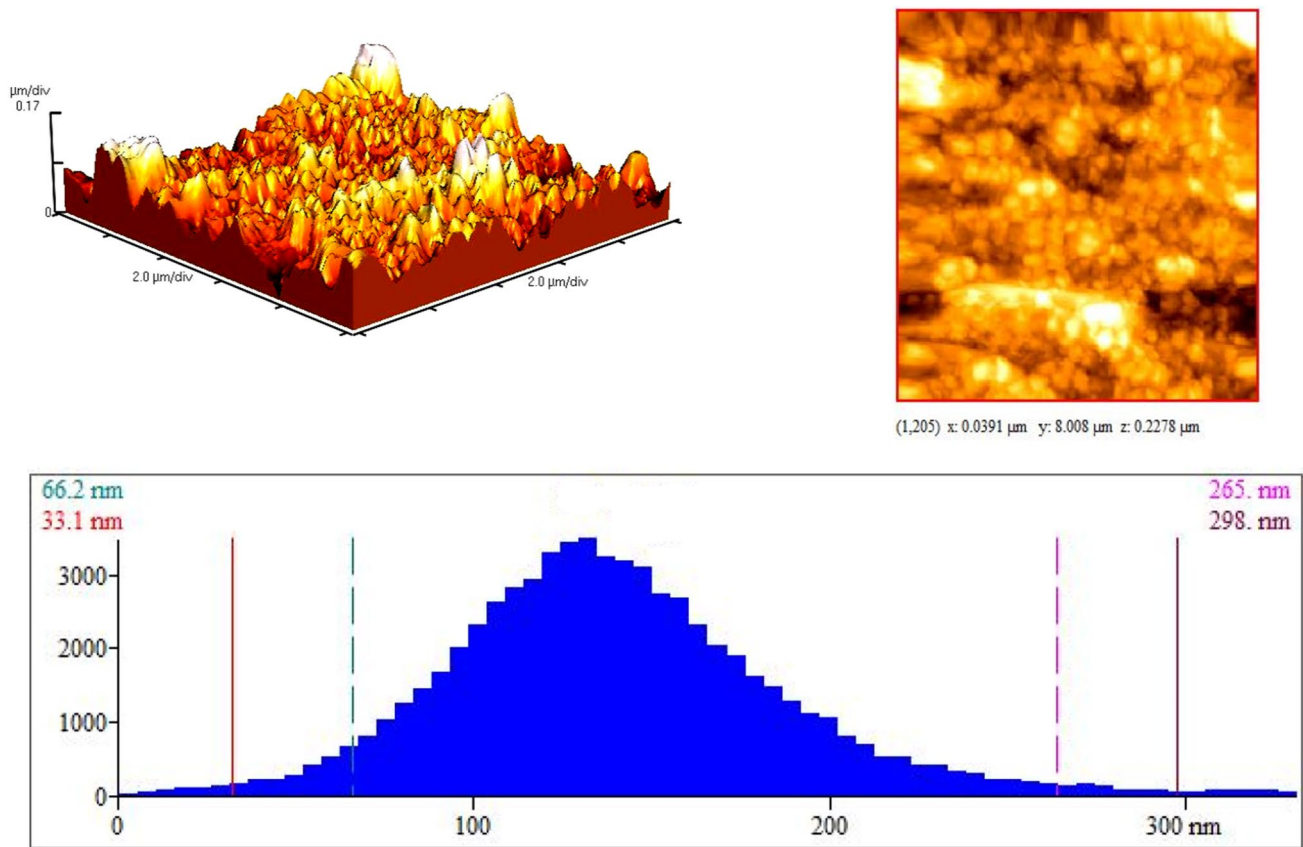


Fig. 12 AFM images of Iron (II, III) oxide/GO, as well as its histogram

varying values of the standard R66 solutions (0, 1, 2, 4, and 4 mL from 100 mg/L dye) were added to each flask. The flasks were then filled with distilled water to the mark line. Then, the flasks were shaken thoroughly until homogenous. The spectrophotometer was used to measure the absorbance of the samples, and a calibration chart was plotted based on the adsorption values of all samples. The line equation was determined using Microsoft Excel, and the unknown sample's concentration (x value) was calculated by setting $y=0$ in the $y=mx+b$ equation. The Iron (II, III) oxide/GO photocatalyst's removal efficiency for the textile wastewater was found to be 90%, as shown in Fig. 18.

BOD and COD analysis

BOD and COD measurements were used as indicators of organic pollution in the textile wastewater. The presence of

dyes in the wastewater is often accompanied by other organic contaminants, such as residual chemicals and organic byproducts from textile manufacturing processes. By measuring BOD and COD, we could assess the overall organic load in the wastewater sample before and after the photocatalytic treatment. A reduction in BOD and COD values after the treatment indicates the degradation and mineralization of organic pollutants, demonstrating the effectiveness of the photocatalytic process in removing organic contaminants.

The Iron (II, III) oxide/GO photocatalyst is an effective solution for the treatment of textile wastewater. Results showed that it can reduce textile wastewater's BOD and COD values from 1910 and 620 mg/L to 19.5 and 27.16 mg/L, respectively. This indicates the removal of organic pollutants, both biodegradable and non-biodegradable, from the wastewater. The results suggest that Iron (II, III) oxide/GO photocatalyst can be a cost-effective and environmentally friendly solution for the treatment of textile wastewater.

Regeneration and recycling of Iron (II, III) oxide/GO

The ability to regenerate and recycle the photocatalyst is crucial in water treatment. In this study, Iron (II, III) oxide/GO was collected after the dye removal reaction and washed

Table 3 The results of AFM analysis

Rp-v (nm)	331.2	Mean Ht (nm)	139.5
Rms rough (nm)	46.55	Median Ht (nm)	135.7
Ave rough (nm)	35.54		

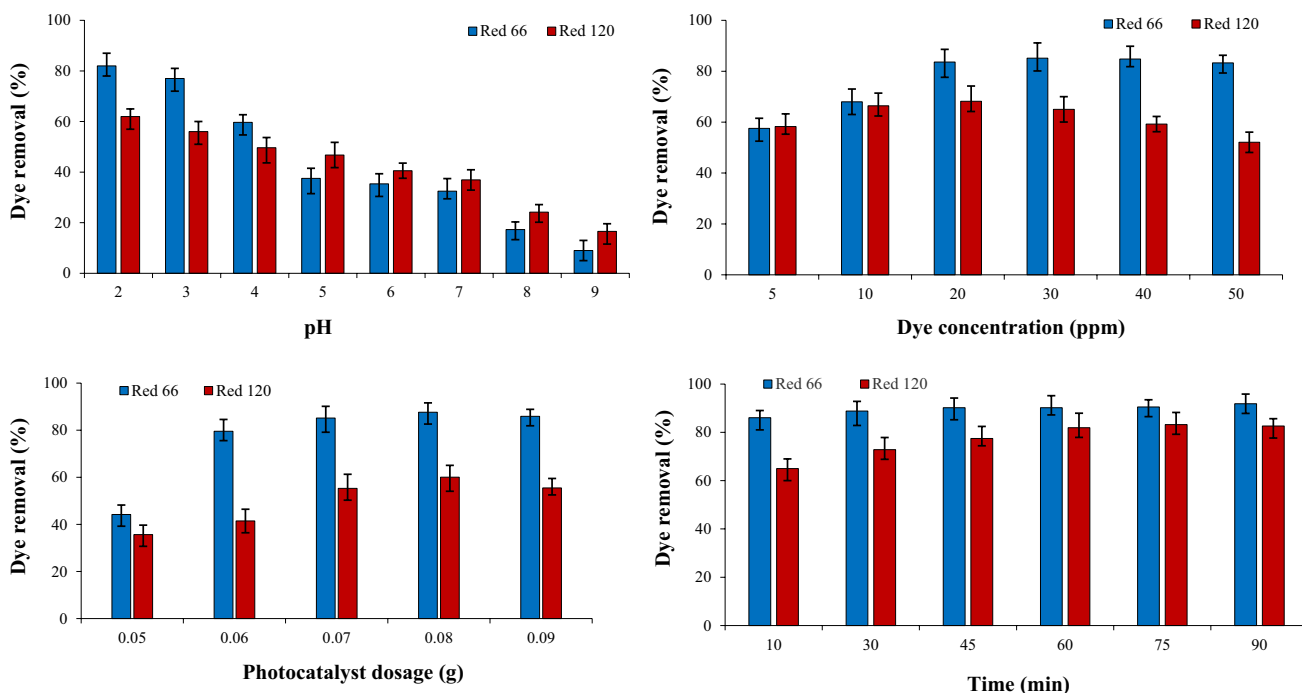


Fig. 13 Effect of pH (2–9), Iron (II, III) oxide dosage (0.05–0.09 g), dye concentration (5–50 mgL⁻¹), and contact time (10–90 min.) on dye removal

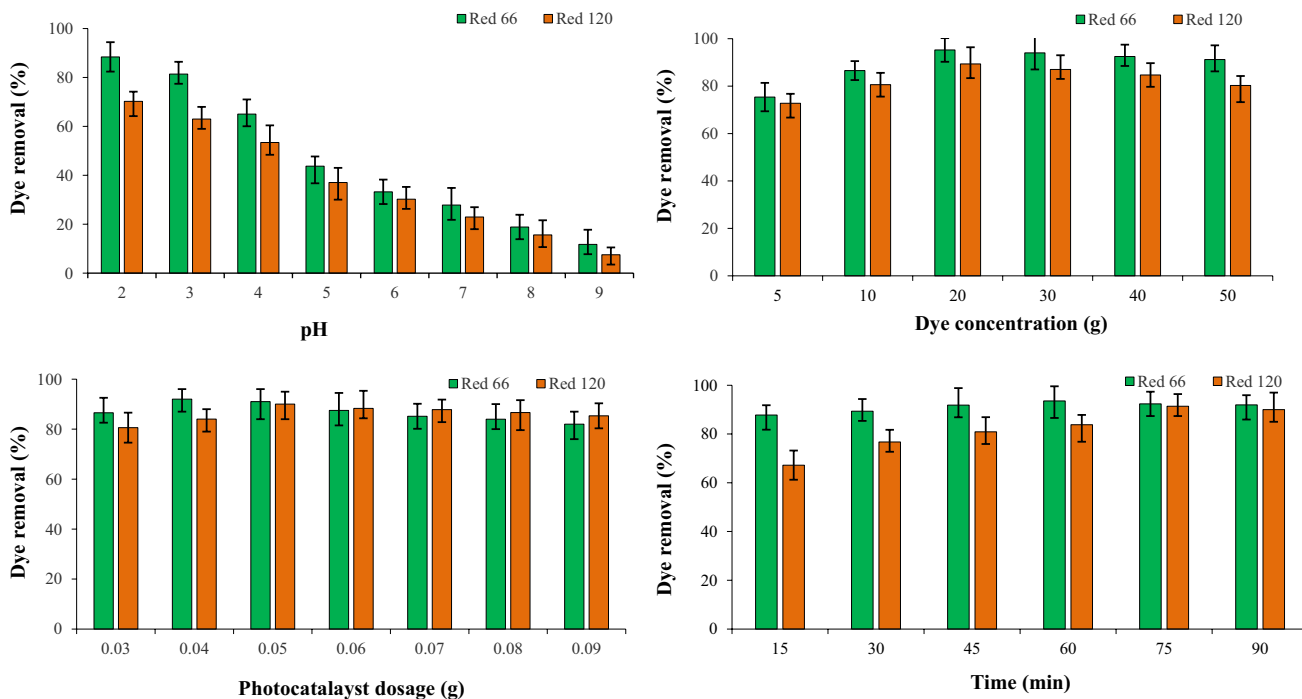


Fig. 14 Effect of pH (2–9), Iron (II, III) oxide/GO dosage (0.03–0.09 g), dye concentration (5–50 mgL⁻¹), and contact time (10–90 min.) on dye removal

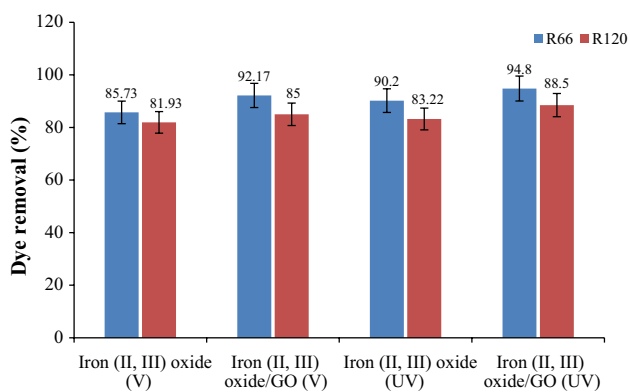


Fig. 15 Dye removal (%) using Iron (II, III) oxide and Iron (II, III) oxide/GO under UV–visible light irradiation

thoroughly with distilled water. The recovered Iron (II, III) oxide/GO was then dried in an oven at 50 °C for 1 h and reused under optimal dye removal conditions. The nanocomposite was used for three cycles to investigate its reusability, and the results are shown in Fig. 18. Notably, the removal percentage remained around 59% and 38% after two cycles (Fig. 19).

Conclusions

This study investigated the photodegradation of Reactive Red 66 and Reactive Red 120 dyes, as well as textile wastewater, under UV and visible light using magnetic oxide nanoparticles and graphene oxide matrix composites. The

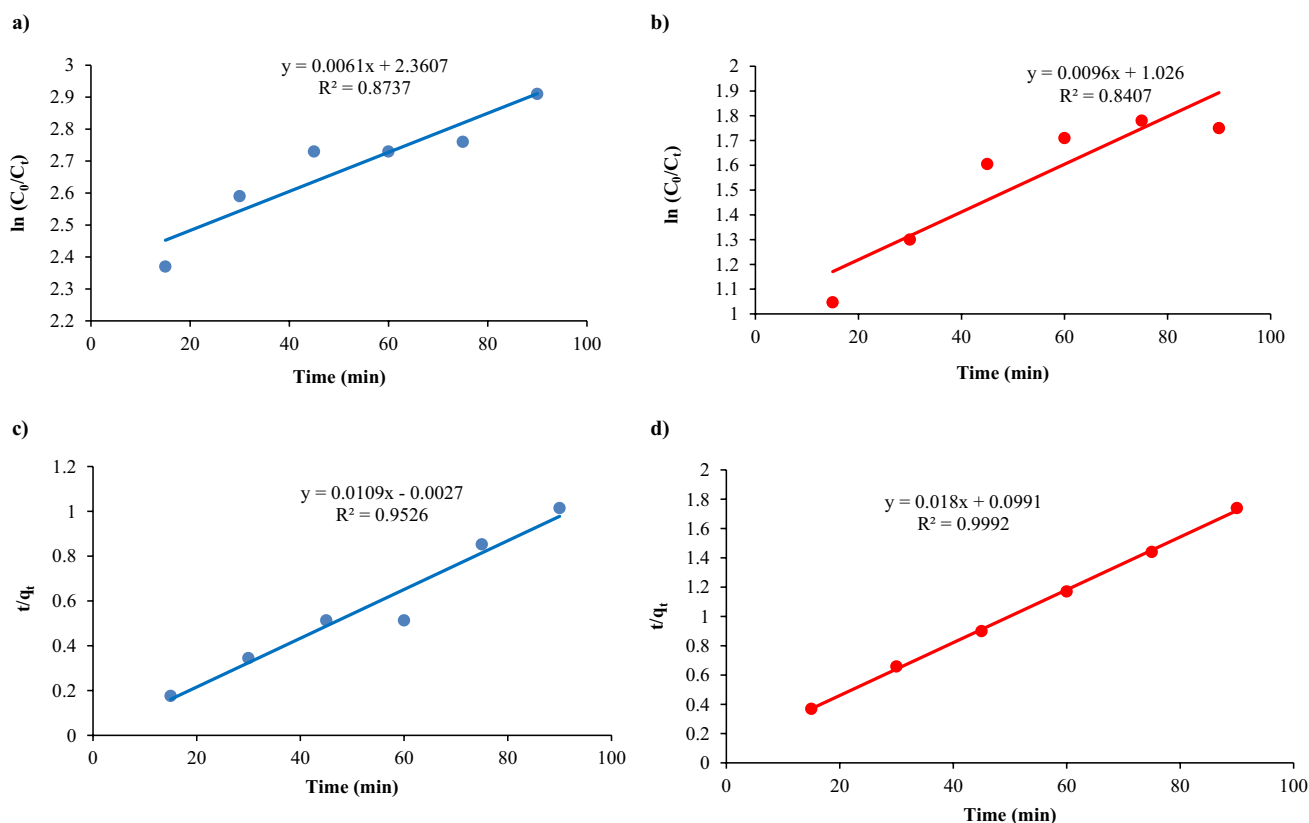


Fig. 16 Kinetic studies of **a, b** Pseudo-first-order and **c, d** Pseudo-second order using Iron (II, III) oxide on Red 66 and Red 120 dyes

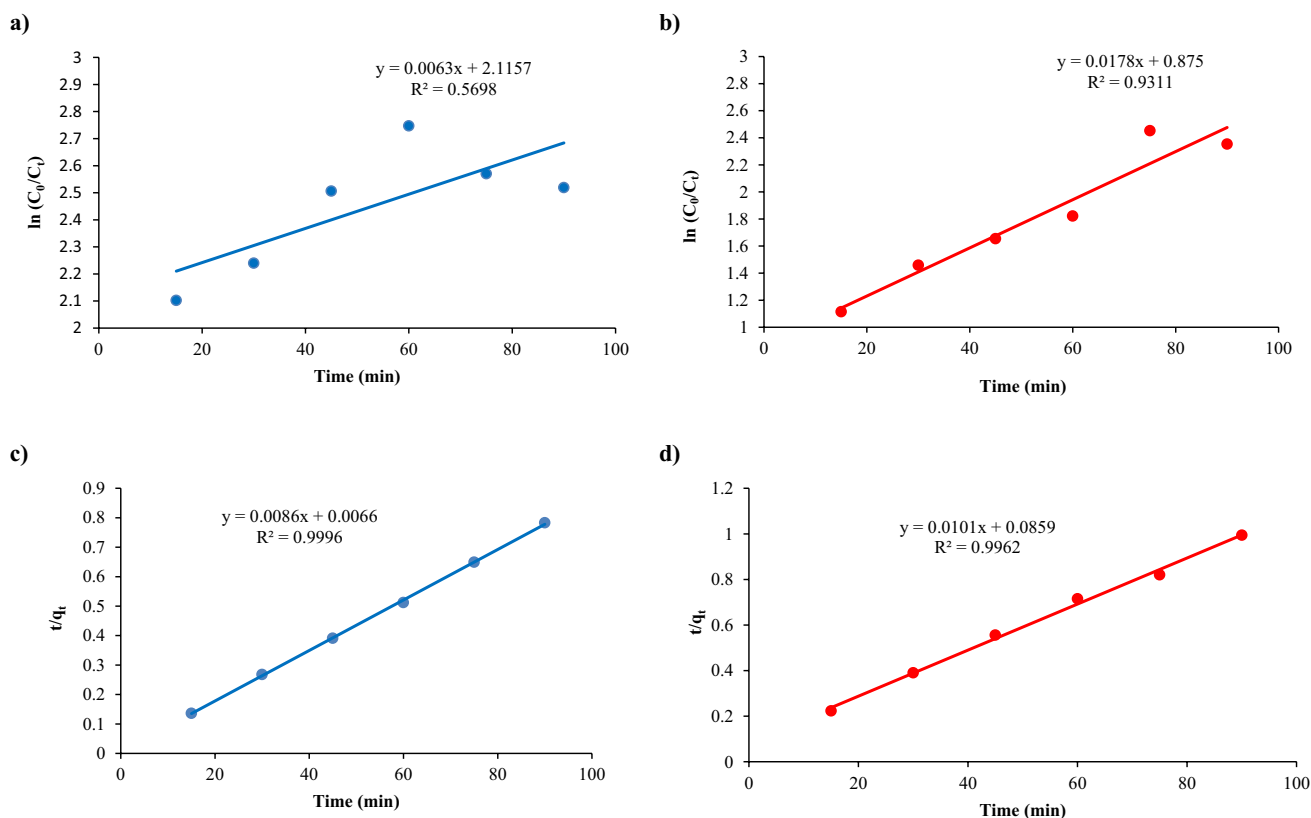


Fig. 17 Kinetic studies of **a, b** Pseudo-first-order and **c, d** Pseudo-second order using Iron (II, III) oxide/GO on Red 66 and Red 120 dyes

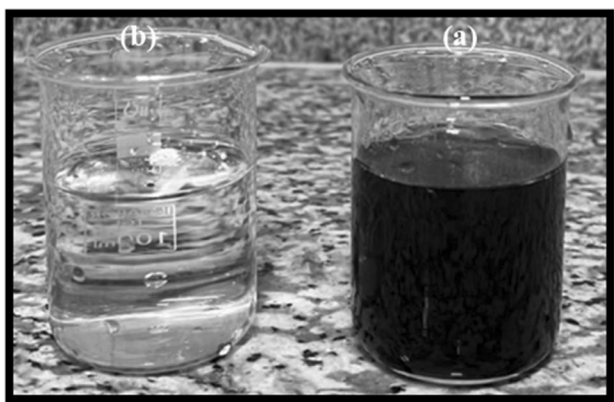


Fig. 18 Photograph of the textile wastewater **a** before and **b** after dye removal

Iron (II, III) and Iron (II, III)/GO photocatalysts were characterized using various techniques such as FT-IR, Raman spectroscopy, XRD, DRS, zeta potential measurements, VSM, SEM, EDAX, and AFM. The results showed that the Iron (II, III) oxide/GO composite had better photocatalytic activity than Iron (II, III) alone, with removal efficiencies of 95.2% and 91.3% for Reactive Red 66 and Reactive Red

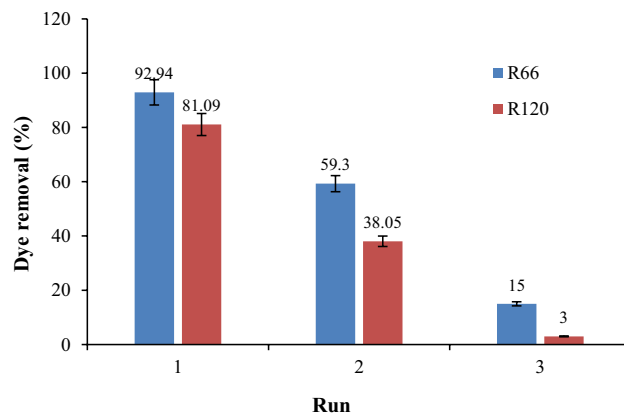


Fig. 19 Reusability investigation of Iron (II, III) oxide/GO towards R66 and R120 dyes removal

120, respectively. The photocatalytic reactions followed the pseudo-second-order model, and the prepared photocatalysts were found to be reusable. The study also demonstrated that the optimized parameters, such as pH value, photocatalyst dosage, initial dye concentration, and irradiation time, played a critical role in enhancing the photodegradation efficiency. Overall, the results suggest that the magnetic

oxide nanoparticle/graphene oxide matrix composite can be an effective and efficient method for the degradation of organic dye pollutants and textile wastewater under UV–visible irradiation.

Declarations

Conflict of interest On behalf of all authors, the corresponding author states that there is no conflict of interest.

References

- Afari M, Masoudpanah SM, Hasheminiyasi M, Alamolhoda S (2023) Effects of iron oxide contents on photocatalytic performance of nanocomposites based on g-C₃N₄. *Sci Rep* 13:6203. <https://doi.org/10.1038/s41598-023-33338-1>
- Aghabozorg H, Zabihi F, Ghadermazi M, Attar Gharamaleki J, Sheshmani S (2006) Piperazinediium bis(pyridine-2,6-dicarboxylato) cuprate(II) tetrahydrate. *Acta Cryst E* 62:m2091–m2093
- Al-Tohamy R, Ali SS, Li F, Okasha KM, Mahmoud YA, Elsamahy T, Jiao H, Fu Y, Sun J (2022) A critical review on the treatment of dye-containing wastewater: ecotoxicological and health concerns of textile dyes and possible remediation approaches for environmental safety. *Ecotoxicol Environ Saf* 231:113160. <https://doi.org/10.1016/j.ecoenv.2021.113160>
- Aragaw TA, Bogale FM, Aragaw BA (2021) Iron-based nanoparticles in wastewater treatment: a review on synthesis methods, applications, and removal mechanisms. *J Saudi Chem Soc* 25(8):101280. <https://doi.org/10.1016/j.jscs.2021.101280>
- Ashori A, Menbari S, Bahrami R (2016) Mechanical and thermo-mechanical properties of short carbon fiber reinforced polypropylene composites using exfoliated graphene nanoplatelets coating. *Ind Eng Chem Res* 38(8):37–42. <https://doi.org/10.1016/j.jiec.2016.04.003>
- Benkhaya S, M'rabet S, Harfi AE (2020) A review on classifications, recent synthesis and applications of textile dyes. *Inorg Chem Commun* 115:107891. <https://doi.org/10.1016/j.inoche.2020.107891>
- Bibi S, Ahmad A, Anjum MAR, Haleem A, Siddiq M, Shah SS, Kahtani AA (2021) Photocatalytic degradation of malachite green and methylene blue over reduced graphene oxide (rGO) based metal oxides (rGO-Fe₃O₄/TiO₂) nanocomposite under UV-visible light irradiation. *J Environ Chem Eng* 9:105580. <https://doi.org/10.1016/j.jece.2021.105580>
- Chen WH, Huang JR, Lin CH, Huang CP (2020) Catalytic degradation of chlorpheniramine over GO-Fe₃O₄ in the presence of H₂O₂ in water: the synergistic effect of adsorption. *Sci Total Environ* 736:139468. <https://doi.org/10.1016/j.scitotenv.2020.139468>
- Díez AG, Rincón-Iglesias M, Lancers-Méndez S, Reguera J, Lizundia E (2022) Multicomponent magnetic nanoparticle engineering: the role of structure-property relationship in advanced applications. *Mater Today Chem* 26:101220. <https://doi.org/10.1016/j.mtchem.2022.101220>
- Dutta S, Gupta B, Srivastava SK, Gupta AK (2021) Recent advances on the removal of dyes from wastewater using various adsorbents: a critical review. *Mater Adv* 2:4497–4531. <https://doi.org/10.1039/D1MA00354B>
- Giri SK, Das NN (2016) Visible light induced photocatalytic decolorisation of rhodamine B by magnetite nanoparticles synthesised using recovered iron from waste iron ore tailing. *Desalin Water Treat* 57:900–907. <https://doi.org/10.1080/19443994.2014.972984>
- Goswami K, Megala U, Kumar SL, Tetala KKR (2023) Synthesis and application of iron based metal organic framework for efficient adsorption of azo dyes from textile industry samples. *Adv Sample Prep* 7:100080. <https://doi.org/10.1016/j.sampre.2023.100080>
- Hosseinian A, Rezaei H, Mahjoub A (2011) Preparation of nanosized iron oxide and their photocatalytic properties for congo red. *World Acad Sci Eng Technol* 5(4):382–385. <https://doi.org/10.5281/zenodo.1328490>
- Hu XD, Zhang HQ, Cao DM (2011) Synthesis of Fe₃O₄ nanocrystals and application in photocatalytic degradation of levofloxacin lactate. *Mater Sci Forum* 688:376–382. <https://doi.org/10.4028/www.scientific.net/MSF.688.376>
- Jiao T, Liu Y, Wu Y, Zhang Q, Yan X, Gao F, Bauer AJP, Liu J, Zeng T, Li B (2015) Facile and scalable preparation of graphene oxide-based magnetic hybrids for fast and highly efficient removal of organic dyes. *Sci Rep* 5:12451
- Kim SH, Choi PP (2017) Enhanced congo red dye removal from aqueous solutions using iron nanoparticles: adsorption, kinetics, and equilibrium studies. *Dalton Trans* 46:15470–15479. <https://doi.org/10.1039/C7DT02076G>
- Kumar B, Smita K, Cumbal L, Debut A, Galeas S, Guerrero VH (2016) Phytosynthesis and photocatalytic activity of magnetite (Fe₃O₄) nanoparticles using the Andean blackberry leaf. *Mater Chem Phys* 179:310–315. <https://doi.org/10.1016/j.matchemphys.2016.05.045>
- Lellis B, Fávoro-Polonio CZ, Pamphile JA, Polonio JC (2019) Effects of textile dyes on health and the environment and bioremediation potential of living organisms. *Biotechnol Res Innov* 3(2):275–290. <https://doi.org/10.1016/j.biori.2019.09.001>
- Li H, Zhao Q, Li X, Zhu Z, Tade M, Liu S (2013) Fabrication, characterization, and photocatalytic property of α -Fe₂O₃/graphene oxide composite. *J Nanopart Res* 15:1670. <https://doi.org/10.1007/s11051-013-1670-x>
- Li Y, Shang S, Shang J, Wang WX (2021) Toxicity assessment and underlying mechanisms of multiple metal organic frameworks using the green algae *Chlamydomonas reinhardtii* model. *Environ Pollut* 291:118199. <https://doi.org/10.1016/j.envpol.2021.118199>
- Mangrulkar PA, Polshettiwar V, Labhsetwar NK, Varma RS, Rayalu SS (2012) Nano-ferrites for water splitting: unprecedented high photocatalytic hydrogen production under visible light. *Nanoscale* 4:5202–5209. <https://doi.org/10.1039/C2NR30819C>
- Mishra PM, Naik GK, Nayak A, Parida KM (2016) Facile synthesis of nano-structured magnetite in presence of natural surfactant for enhanced photocatalytic activity for water decomposition and Cr (VI) reduction. *Chem Eng J* 299:227–235. <https://doi.org/10.1016/j.cej.2016.04.052>
- Naik SS, Lee SJ, Theerthagiri J, Yu Y, Choi MY (2021) Rapid and highly selective electrochemical sensor based on ZnS/Au-decorated f-multi-walled carbon nanotube nanocomposites produced via pulsed laser technique for detection of toxic nitro compounds. *J Hazard Mater* 418:126269. <https://doi.org/10.1016/j.jhazmat.2021.126269>
- Park B, Kim BH, Yu T (2018) Synthesis of spherical and cubic magnetic iron oxide nanocrystals at low temperature in air. *J Colloid Interface Sci* 518:27–33. <https://doi.org/10.1016/j.jcis.2018.02.026>
- Pervez MN, He W, Zarra T, Naddeo V, Zhao Y (2020) New sustainable approach for the production of Fe₃O₄/graphene oxide-activated persulfate system for dye removal in real wastewater. *Water* 12(3):733. <https://doi.org/10.3390/w12030733>
- Poh HL, Sanek F, Ambrosi A, Zhao G, Sofer Z, Pumer M (2012) Graphenes prepared by staudenmaier, hofmann and hummers methods with consequent thermal exfoliation exhibit very different

- electrochemical properties. *Nanoscale* 4:3515. <https://doi.org/10.1039/c2nr30490b>
- Rabbani M, Rafiee F, Ghafari H, Rahimi R (2015) Synthesis of Fe₃O₄ nanoparticles via a fast and facile mechanochemical method: modification of surface with porphyrin and photocatalytic study. *Mater Lett* 166:247–250. <https://doi.org/10.1016/j.matlet.2015.12.087>
- Reza KM, Kurny A, Gulshan F (2016) Photocatalytic degradation of methylene blue by magnetite+H₂O₂+UV process. *Int J Environ Sci Dev* 7:325–329. <https://doi.org/10.7763/IJESD.2016.V7.793>
- Samsami S, Mohamadizani M, Sarrafzadeh MH, Rene ER, Firoozbahr M (2020) Recent advances in the treatment of dye-containing wastewater from textile industries: overview and perspectives. *Process Saf Environ Prot* 143:138–163. <https://doi.org/10.1016/j.psep.2020.05.034>
- Shebanova ON, Lazor P (2003) Raman study of magnetite (Fe₃O₄) laser-induced. *J Raman Spectrosc* 34:845–852. <https://doi.org/10.1002/jrs.1056>
- Sheshmani S (2013) Effects of extractives on some properties of bagasse/high density polypropylene composite. *Carbohydr Polym* 94(1):416–419. <https://doi.org/10.1016/j.carbpol.2013.01.067>
- Sheshmani S, Nayebi M (2019) Modification of TiO₂ with graphene oxide and reduced graphene oxide; enhancing photocatalytic activity of TiO₂ for removal of remazol Black B. *Polym Compos* 40(1):210–216. <https://doi.org/10.1002/pc.24630>
- Sheshmani S, Falahat B, Nikmaram FR (2017) Preparation of magnetic graphene oxide-ferrite nanocomposites for oxidative decomposition of Remazol Black B. *Int J Biol Macromol* 97:671–678. <https://doi.org/10.1016/j.ijbiomac.2017.01.041>
- Soleimannejad J, Sharif M, Sheshmani S, Alizadeh R, Moghimi A, Aghabozorg H (2005) Crystal structure of a proton-transfer self-associated compound from 1,10-phenanthroline-2,9-dicarboxylic acid and creatinine. *Anal Sci* 21:x49–x50
- Solomon RV, Lydia IS, Merlin JP, Venuvanalingam P (2012) Enhanced photocatalytic degradation of azo dyes using nano Fe₃O₄. *J Iran Chem Soc* 9:101–109. <https://doi.org/10.1007/s13738-011-0033-8>
- Suresh R, Udayabhaskar R, Sandoval C, Ramirez E, Mangalaraja RV, Mansilla HD, Contreras D, Yáñez J (2018) Effect of reduced graphene oxide on the structural, optical, adsorption and photocatalytic properties of iron oxide nanoparticles. *New J Chem* 42:8485–8493. <https://doi.org/10.1039/C8NJ00321A>
- Theerthagiri J, Lee SJ, Karuppasamy K, Arulmani S, Veeralakshmi S, Ashokkumar M, Choi MY (2021) Application of advanced materials in sonophotocatalytic processes for the remediation of environmental pollutants. *J Hazard Mater* 412:125245. <https://doi.org/10.1016/j.jhazmat.2021.125245>
- Theerthagiri J, Park J, Das HT, Rahamathulla N, Cardoso ESF, Murthy AP, Maia G, Vo DVN, Choi MY (2022) Electrocatalytic conversion of nitrate waste into ammonia: a review. *Environ Chem Lett* 20:2929–2949. <https://doi.org/10.1007/s10311-022-01469-y>
- Tung WS, Daoud WA (2009) New approach toward nanosized ferrous ferric oxide and Fe₃O₄-doped titanium dioxide photocatalysts. *ACS Appl Mater Interfaces* 1:2453–2461. <https://doi.org/10.1021/am900418q>
- Villegas VAR, Ramírez JIDL, Guevara EH, Sicairos SP, Ayala LAH, Sanchez BL (2020) Synthesis and characterization of magnetite nanoparticles for photocatalysis of nitrobenzene. *J Saudi Chem Soc* 24:223–235. <https://doi.org/10.1016/j.jscs.2019.12.004>
- Vinodhkumar G, Wilson J, Inbanathan SS, Potheher IV, Ashokkumar M, Peter AC (2020) Solvothermal synthesis of magnetically separable reduced graphene oxide/Fe₃O₄ hybrid nanocomposites with enhanced photocatalytic properties. *Phys B Condens* 580:411752. <https://doi.org/10.1016/j.physb.2019.411752>
- Wang G, Chen G, Wei Z, Dong X, Qi M (2013) Multifunctional Fe₃O₄/graphene oxide nanocomposites for magnetic resonance imaging and drug delivery. *Mater Chem Phys* 141(2–3):997–1004. <https://doi.org/10.1016/j.matchemphys.2013.06.054>
- Wang W, He Q, Xiao K, Zhu L (2018) Electrostatic self-assembly of Fe₃O₄/GO nanocomposites and their application as an efficient Fenton-like catalyst for degradation of rhodamine B. *Mater Res Express* 5(3):035510. <https://doi.org/10.1088/2053-1591/aab2dc>

Publisher's Note Springer Nature remains neutral with regard to jurisdictional claims in published maps and institutional affiliations.

Springer Nature or its licensor (e.g. a society or other partner) holds exclusive rights to this article under a publishing agreement with the author(s) or other rightsholder(s); author self-archiving of the accepted manuscript version of this article is solely governed by the terms of such publishing agreement and applicable law.